Computational Materials Science II

PROGRESS REPORT # 3

Vourvachakis S. Georgios
mse354

April 8, 2025

Contents

—— 1 ——

INTRODUCTION

In the context of crystalline materials, the ground state configuration corresponds to the atomic arrangement at which the total energy of the system is minimized. Formally, this is formulated as a variational problem. In density functional theory (DFT), one seeks the electron density $\rho(r)$ that minimizes the energy functional[1][SS11]

$$E[\mathbf{r}; \rho] := T[\rho] + V_{\text{ext}}[\mathbf{r}; \rho] + E_{\text{HF}}[\mathbf{r}; \rho] + E_{\text{XC}}[\mathbf{r}; \rho] \text{ , subject to } \int_{\mathcal{V}} \rho(\mathbf{r})d\mathbf{r} = N \text{ ,}$$

where N is the number of electrons in the system. For a periodic system, the minimization is often performed per atom, with the *energy per atom* $\epsilon_t = \frac{E_t}{N_a}$ plotted against the *volume per atom v*. The so-called *universal binding curve* illustrates that as atoms are brought together, the energy per atom decreases until a minimum (the equilibrium state) is reached; further compression leads to an increase in energy. This variational minimization is central to finding the equilibrium lattice constants of a crystal.[Sab13]

The lattice constant (or constants, for anisotropic structures) defines the periodicity and size of the unit cell in a crystal. Within DFT calculations, one typically computes the total energy for various lattice parameters, fitting the energy versus volume (or lattice constant) curve with a suitable equation of state (EOS) to locate the minimum energy configuration.[Sch+23]

The universal binding curve describes the dependence of the energy per atom ϵ_t on the atomic volume v. Near the minimum, the energy can be approximated by a Taylor expansion. For example, assuming a quadratic (second-order) behavior (*parabolic approximation*):

$$E(a) = E_0 + \frac{1}{2} \frac{d^2 E(a)}{d^2 a}\bigg|_{a=a_0} (a - a_0)^2 + O((a - a_0)^3) \text{ ,}$$

where a represents the lattice constant (or a suitable geometric parameter), and a_0 is its equilibrium value. This expansion is justified in the vicinity of the minimum, where higher-order terms become negligible.

Of course, by the multivariate extension of Taylor's expansion, one can generalize the aforementioned approximation for higher degrees of freedom (e.g., in HCP, a multivariate minimization is performed for the spatially-dependent energy function with respect to a and c).

Definition . (Multivariate version of Taylor's theorem)[Kön06] Let $f : \mathbb{R}^n \mapsto \mathbb{R}$ be a k-times *continuously differentiable* function at the point-origin $\mathbf{q} \in \mathbb{R}^n$. Then there exist functions $h_a : \mathbb{R}^n \mapsto \mathbb{R}$, where $|a| = k$, such that

$$f(\mathbf{x}) = \sum_{|a| \leq k} \frac{D^a f(\mathbf{q})}{a!} (\mathbf{x} - \mathbf{q})^a + \sum_{|a|=k} h_a(\mathbf{x})(\mathbf{x} - \mathbf{q})^a \text{, and } \lim_{\mathbf{x} \to \mathbf{q}} h_a(\mathbf{x}) = 0 \text{ ,}$$

---

[1]For a more thorough analysis of the *variational optimization framework* under the Hohenberg-Kohn theorems and Kohn-Sham equations, refer to assignment 1.

where the shorthand $D^a f$ denotes the higher order derivatives:

$$D^a f \equiv \frac{\partial^{|a|} f}{\partial \mathbf{x}^a} = \frac{\partial^{a_1 + \cdots + a_n} f}{\partial x_1^{a_1} \cdots \partial x_n^{a_n}} \, .$$

1.1 THE BIRCH–MURNAGHAN EQUATION OF STATE

The Birch–Murnaghan isothermal equation of state, published in 1947 by Albert Francis Birch[Bir47] is a relationship between the volume of a body and the pressure to which it is subjected. Birch proposed this equation based on the work of Francis Dominic Murnaghan in 1944[Mur44] so that the equation is named in honor of both scientists.

The bulk modulus B is a measure of a material's resistance to uniform compression. It is defined as

$$B = -V \frac{dP}{dV} \bigg|_T = V \frac{d^2 E}{dV^2} \bigg|_T \, ,$$

evaluated at the equilibrium volume V_0. For crystalline structures, a convenient variable is the lattice constant α. In the case of an FCC crystal, for instance, the volume per atom is given by $V = \frac{\alpha^3}{4}$, thus $\frac{dV}{d\alpha} = \frac{3\alpha^2}{4}$, and $\frac{d^2 V}{d\alpha^2} = \frac{3\alpha}{2}$. Invoking the univariate Leibniz's rule, the second derivative of the energy with respect to α is

$$\frac{d^2 E}{d\alpha^2} = \frac{d^2 E}{dV^2} \left(\frac{dV}{d\alpha} \right) + \frac{dE}{dV} \frac{d^2 V}{d\alpha^2} \, .$$

and at equilibrium ($\frac{dE}{dV} \big|_{V_0} = 0$),

$$\frac{d^2 E}{d\alpha^2} = \left(\frac{3\alpha^2}{4} \right)^2 \frac{d^2 E}{dV^2} = \frac{9\alpha^4}{16} \frac{d^2 E}{dV^2} \, .$$

Solving for $\frac{d^2 E}{dV^2}$ yields

$$\frac{d^2 E}{dV^2} = \frac{16}{9\alpha^4} \frac{d^2 E}{d\alpha^2} \, .$$

Substituting this into the definition of the bulk modulus,

$$B = V \frac{d^2 E}{dV^2} = \frac{\alpha^3}{4} \cdot \frac{16}{9\alpha^4} \frac{d^2 E}{d\alpha^2} = \frac{4}{9\alpha} \frac{d^2 E}{d\alpha^2} \, .$$

Thus, the bulk modulus in terms of the lattice constant α near the equilibrium α_0 is given by

$$B \coloneqq \frac{4}{9\alpha_0} \frac{d^2 E}{d\alpha^2} \bigg|_{\alpha = \alpha_0} \, ,$$

which is the final expression used in our theoretical estimates. This derivation—originating from the Murnaghan EOS and its subsequent developments—provides a clear connection between the curvature of the energy curve at equilibrium and the elastic response of the material.[Mur44]

1.2 STRUCTURE OPTIMIZATION AND STRESS TENSOR ANALYSIS

When constructing crystal lattices for DFT calculations, one typically uses prototype structures. For instance, the FCC and BCC structures have well-defined primitive vectors and basis vectors. For FCC, the primitive vectors may be expressed as

$$\alpha_1 = \frac{1}{2}\alpha(\mathbf{y} + \mathbf{z}),$$
$$\alpha_2 = \frac{1}{2}\alpha(\mathbf{x} + \mathbf{z}),$$
$$\alpha_3 = \frac{1}{2}\alpha(\mathbf{x} + \mathbf{y}),$$

with a single basis atom at the origin. Similar expressions exist for BCC structures. For HCP structures, two lattice parameters, α and c, must be determined, with the ideal ratio often estimated from the nearest neighbor distances in FCC crystals.

After constructing the initial guess for the lattice geometry, a two-parameter fit is usually employed. The stress tensor, which quantifies the forces acting on the lattice due to small deformations, is computed. The optimization process uses methods such as the Broyden–Fletcher–Goldfarb–Shanno (BFGS) algorithm [Fle88], which iteratively updates the structure by making use of the Hessian matrix H defined by

$$H_{ij} \coloneqq \frac{\partial^2 E}{\partial x_i \partial x_j},$$

and approximates the energy change as

$$\delta E = \frac{1}{2}(\mathbf{x} - \mathbf{x}_{\min})^\top H (\mathbf{x} - \mathbf{x}_{\min}).$$

This strategy efficiently converges toward the minimum energy configuration by incorporating the local curvature of the energy landscape.

1.3 IMPLEMENTATION WITH GPAW AND PLANE WAVE BASIS

In particular GPAW—a real-space, projector augmented-wave (PAW) code— is widely used to perform these DFT calculations. GPAW implements the stress tensor evaluation, allowing for a robust structure optimization process. The convergence tests—adjusting k-point sampling and the plane wave cutoff—are critical to ensure that the calculated lattice constants and bulk moduli are accurate. Detailed examples of this implementation can be found in the GPAW tutorials and in the ASE tutorials for lattice constant determination.

In our project, these methods are applied to analyze (hexagonal) 2H-WTe$_2$ [WDW23]. We begin with an initial guess for the equilibrium structure using prototypical lattice builders, then refine the structure by testing convergence parameters. Finally, we compare our theoretical lattice constants and elastic properties—such as the bulk modulus—with experimental data.

Each of these topics is crucial for a comprehensive understanding of the mechanical stability and response of crystalline materials, and the methods described here form the backbone of modern computational materials science.

2

STRUCTURAL ANALYSIS OF ALUMINUM

Aluminum naturally crystallizes in a face-centered cubic (FCC) structure with an experimental lattice constant of approximately 4.0495Å[SW71]. Under extreme pressures, aluminum is predicted to transition into a body-centered cubic (BCC) phase. The lattice constant in metallic crystals is directly linked to the atomic packing factor (APF): for FCC, the APF is 74.05%, while for BCC it is 68%. This difference implies that, given the same atomic radius, the FCC structure will pack atoms more efficiently and thus feature a smaller lattice constant relative to the BCC structure.

For our computational investigations using density functional theory (DFT) with GPAW, the primitive cell vectors for each structure are defined as follows:

- For FCC:

$$\mathbf{v}_1 = [0, b, b] \,,$$
$$\mathbf{v}_2 = [b, 0, b] \,,$$
$$\mathbf{v}_3 = [b, b, 0] \,,$$

with $b = \frac{\alpha}{2}$ (fig.1).

- For BCC;

$$\mathbf{v}_1 = [-b, b, b] \,,$$
$$\mathbf{v}_2 = [b, -b, b] \,,$$
$$\mathbf{v}_3 = [b, b, -b] \,,$$

with $b = \frac{\alpha}{2}$ (fig.2).

Here, α denotes the lattice constant, which is optimized in subsequent steps.
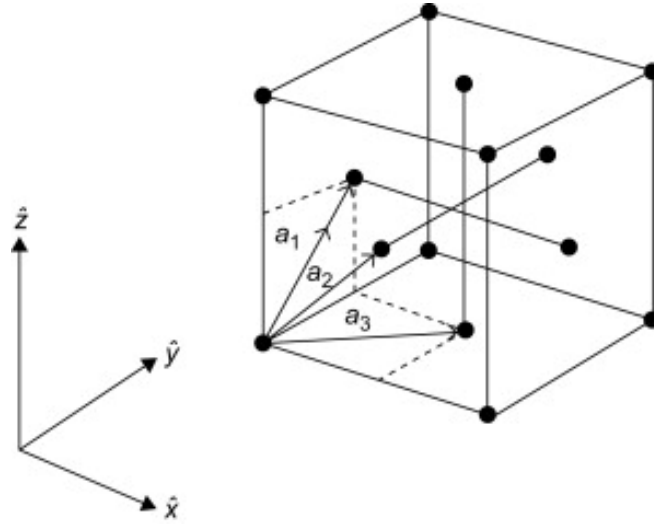
Figure 1: Symmetric set of primitive vectors for the fcc Bravais lattice. They form the rhombohedral primitive cell of the FCC crystal. The primitive vectors $\mathbf{a}_1$, $\mathbf{a}_2$, $\mathbf{a}_3$ connect the lattice points at the face centers. [Mis12]
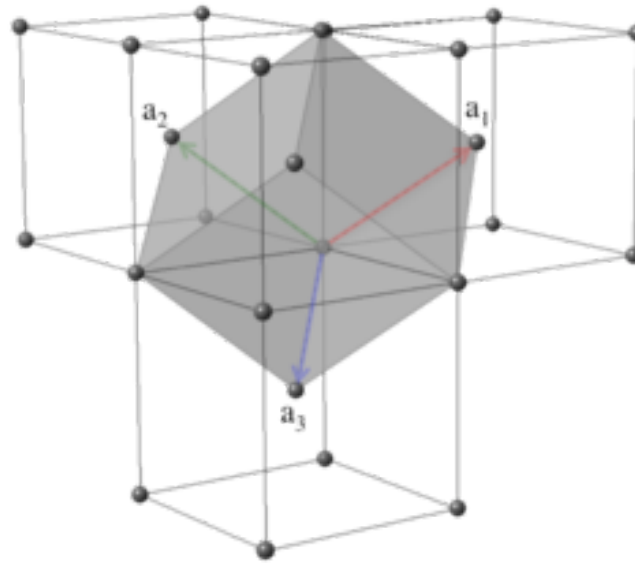
Figure 2: Primitive translation vectors of the BCC lattice; these vectors connect the lattice point at the origin to lattice points at the body centers. The primitive cell is obtained on completing the rhombohedron.[Mis12]

2.1   K-POINT CONVERGENCE STUDY

A robust DFT calculation requires ensuring that the integration over the Brillouin zone is well converged. We performed a series of calculations using k-point grids increasing in density from 2 × 2 × 2 up to 10 × 10 × 10. Energy values are plotted as a function of the k-point grid density, and the "elbow point"—where further increasing the grid density yields negligible improvement in energy—is identified. For our aluminum calculations (see fig.3):

- The FCC phase shows convergence at a grid of approximately $4 \times 4 \times 4$ or `k_elbow=4`.
- The BCC phase requires a denser grid, converging near $7 \times 7 \times 7$ or `k_elbow=7`.

This convergence study ensures that our total energy calculations are accurate and reliable for further structural optimization.
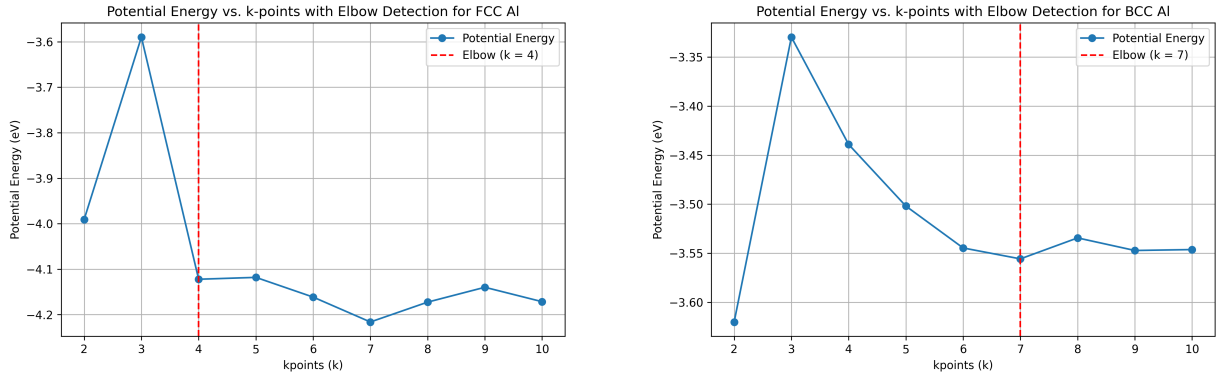

Figure 3: Potential Energy vs. k-points graphs for FCC and BCC aluminum respectively, with "elbow detection" markers. For FCC, the elbow is detected at $k = 4$ (right panel), while for BCC, it's at $k = 7$ (left panel). These graphs show how the calculated potential energy converges as the k-point sampling density increases. Both structures show an initial rise in energy at $k = 3$ followed by stabilization.

2.2   LATTICE PARAMETER OPTIMIZATION

Once the optimal k-point density is determined, the next step is to optimize the lattice constant. For each crystal structure:

- FCC: Calculations are performed over a range of lattice constants around 4.05 Å (±2% variation).
- BCC: Given the expected larger lattice constant due to the lower APF, we explore a broader range (±10% variation) around an estimated value.

The potential energy is fitted using a quadratic polynomial, $E(\alpha) = a_2 \alpha^2 + a_1 \alpha + a_0$, and the minimum is located by differentiating, $\alpha_{\min} = -\frac{a_1}{2a_2}$. This parabolic fit, illustrated in fig.4, allows us to extract both the equilibrium lattice constant and the curvature necessary to determine the bulk modulus.
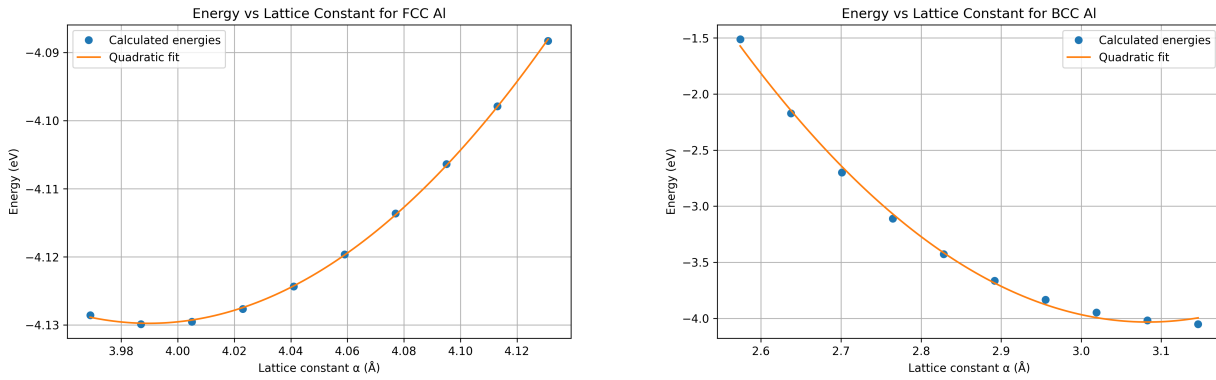
Figure 4: Energy vs lattice constant plots for FCC and BCC aluminum. The FCC graph shows a shallow parabolic curve with a minimum around 4.0 Å, while the BCC graph shows a deeper curve with a minimum near 3.1 Å. Both include quadratic fit lines that match optimally the calculated energy points.

2.3 DATA ANALYSIS AND BULK MODULUS CALCULATION

With the fitted polynomial, the bulk modulus is calculated from the curvature at the minimum using eq.1.1:

$$B = \frac{4}{9\alpha_0} \times 2a_2 \ .$$

A conversion factor of 160.21766 is applied to convert the units from $eV/\text{Å}^2$ to GPa. The calculated bulk moduli are then compared with experimental values:

- **FCC Aluminum:**
    1. Fitted minimum at $\alpha \approx 3.990$Å gives $B \approx 74.69$ GPa (1.98% error relative to the experimental 76.2 GPa [TW79]).
    2. Using the theoretical value [SW71], $\alpha_0 = 4.050$, yields $B \approx 73.58$ (3.44% error of theoretical with respect to the experimental estimate).

- **BCC Aluminum:**
    1. Fitted minimum at $\alpha \approx 3.083$Å gives $B \approx 438.29$ GPa (7.73% error relative to the experimental 475.0 GPa [Pol+17],[ZWL25]).
    2. Using the theoretical value [SW71], $\alpha_0 = 2.860$, yields $B \approx 472.51$ GPa (0.52% error divergence of theoretical to experimental measurement).

These results illustrate the sensitivity of the bulk modulus to the precise value of the lattice constant and validate our computational approach against experimental benchmarks.

2.3.1   On the Lattice Parameters Estimation

Given that the FCC phase packs atoms more densely (APF of 74.05%), one might initially expect the BCC phase to have a larger lattice constant for the same atomic radius. However, our analysis shows that while the empirical estimation based on APF suggests a larger lattice constant for BCC, the actual energy minimization reveals a more complex picture. The theoretical prediction for BCC (with a minimum at $\alpha \approx 3.083$Åor 2.860 Å, depending on the approach) indicates that other factors, such as electron distribution and bonding characteristics under high pressure, play a significant role.

2.3.2   Comparison of Energy per Atom in FCC vs. BCC Aluminum

The energy versus lattice constant plots (fig.4) for FCC and BCC aluminum exhibit distinct features. The FCC structure displays a shallow energy well with a minimum near 4.0 Å, indicative of the naturally stable configuration under ambient conditions. Conversely, the BCC structure shows a deeper energy well with a minimum near 3.1 Å(or closer to 2.86 Åwhen using experimental benchmarks), suggesting that while BCC aluminum is *metastable under standard conditions*, it becomes favorable only under *extreme pressures*. The lower energy per atom in the FCC phase confirms why aluminum is naturally observed in this configuration, whereas the BCC phase, despite its potentially higher stiffness (as reflected in the significantly higher bulk modulus), is accessible only through high hydrostatic pressure conditions. Specifically, Aluminum undergoes sequential phase transitions under ramp compression: FCC → HCP at 216±9 GPa and HCP → BCC at 321± 12 GPa [Yu+23]. The BCC phase persists up to 475 GPa, the highest pressure tested [Pol+17]. Crystallographic texture analysis shows that close-packed planes (e.g., FCC (111), BCC (110)) remain parallel during transitions [He+22].

In this section we presented a gradual and systematic approach to analyzing the structural properties of aluminum in both FCC and BCC phases. By defining the crystal structures, ensuring k-point convergence, optimizing the lattice parameters, and performing detailed energy analysis, we can extract the structural parameters and elastic properties of crystalline materials. The results not only validate our computational methodology but also highlight the inherent differences in stability and mechanical response between the FCC and BCC phases of aluminum.
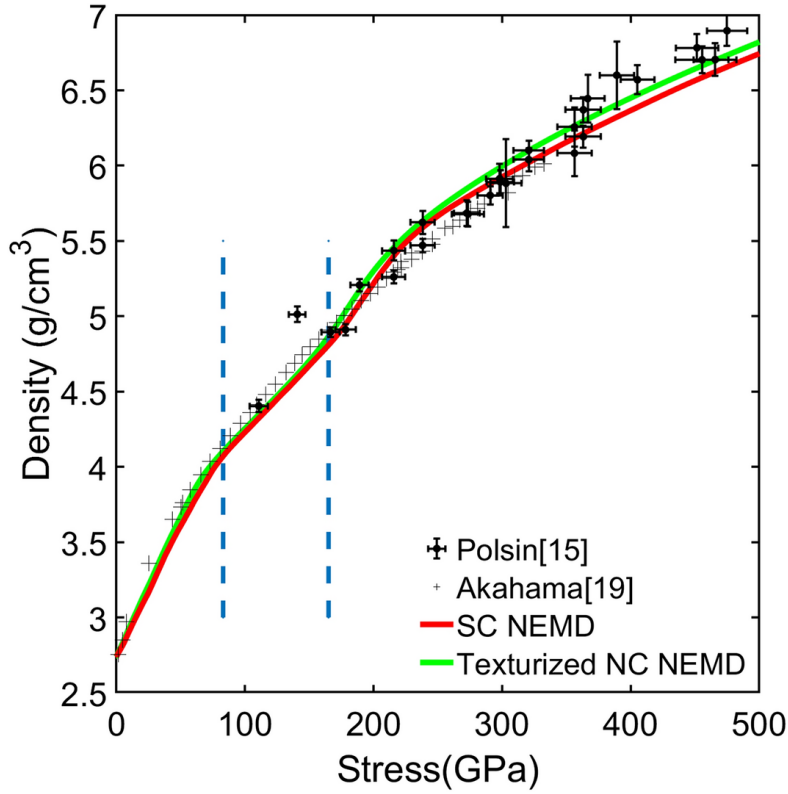
Figure 5: Density–stress curves for different simulation setups. The data are compared with ramp experiment from Polsin et al. [Pol+17] and diamond anvil cell data by Akahama et al. [Aka+06]. For both the simulation data and experiment data, the stress and density refers to the average stress and density throughout the thickness of the entire Al domain as a function of time, which is referred to as the *global stress and density* on the study in He et al. [He+22]. The first vertical dashed bar denotes the pressure onset for 100% bcc in single crystal (SC) non-equilibrium molecular dynamics (NEMD). In between the two vertical dashed bars, the structure is full bcc and deforming elastically for SC NEMD. After the second dashed bars, defect growth is observed in SC NEMD.

3

VOLUME-BASED APPROACH AND ASE EQUATION OF STATE

In this formulation, rather than directly varying the lattice constant, the computational framework systematically varies the crystal volume in the vicinity of the equilibrium configuration. This approach is based on the following considerations.

- Non-linear Relationship Between Lattice Constant and Volume: For a cubic system, the volume scales as the cube of the lattice constant aa (i.e., $V \propto \alpha^3$). This nonlinearity necessitates a volume-based sampling strategy, as direct linear variations in α do not correspond to uniform changes in volume.

- Consistent Volume Sampling: The sampling is defined over a relative variation range—for example, ±10% for FCC and ±15% for BCC—ensuring that the data points are distributed uniformly in terms of the physical volume. This uniformity improves the quality of the EOS fitting process.

The ASE (Atomic Simulation Environment) library provides a robust built-in functionality to fit the energy–volume data using an EOS model, specifically the Murnaghan isothermal EOS [Mur44][2]

1. **Physical Accuracy:** The Murnaghan EOS is known to capture the non-linearity of the energy–volume relationship better than a simple quadratic polynomial. It automatically extracts parameters such as the equilibrium volume V_0, equilibrium energy E_0, and the bulk modulus B.

2. **Automation and Robustness:** By integrating the EOS functionality within the workflow, the need for manual quadratic fitting is eliminated, reducing the potential for human error. Additionally, ASE offers integrated plotting capabilities to visualize the fit, enhancing the diagnostic process.

3. **Enhanced DFT Parameters:** Consistent parameters—such as a plane-wave cutoff of 300 eV, Fermi–Dirac smearing for electronic convergence, and a double-zeta polarized (dzp) basis set[AS03]—are maintained to ensure reliable comparisons between the FCC and BCC phases.

3.1 RELATIVE VOLUME VARIATION FROM LATTICE CONSTANT VARIATION

Given a nominal lattice constant α_0 for a cubic lattice, a relative variation in α can be expressed as:

$$\alpha = \alpha_0 \left(1 \pm p_\alpha\right),$$

where $p_\alpha := \frac{|\alpha - \alpha_0|}{\alpha_0}$ represents the relative change in the lattice constant.

we need to compute the equivalent variation for the cubic volume per atom p_V, where $p_V := \frac{|V - V_0|}{V_0}$.

Based on the expression for α, the corresponding volume V is

$$V = \alpha^3 = \alpha_0^3 (1 \pm p_\alpha)^3.$$

The absolute change in volume is $|V - V_0| = \alpha_0^3 |(1 \pm p_a)^3 - 1|$.

Thus, the relative volume variation p_V is given by:

$$p_V = \left|(1 \pm p_\alpha)^3 - 1\right|.$$

---

[2] Note that the Birch-Murnaghan equation of state (EOS) [Bir47] is different from the Murnaghan EOS.

The energy-volume relationship for Murnaghan isotherm is:

$$E(V) = E_0 + \left(\frac{B_0 V_0}{B_0'}\right) \left[\frac{(V/V_0)^{-B_0'}}{B_0' - 1}\right] - \frac{B_0 V_0}{B_0' - 1},$$

under linear variation of bulk modulus with pressure ($B = B_0 + B_0' P$), where B_0 is the *modulus of incompressibility* and $B_0' := \frac{\partial B_0}{\partial P}\Big|_T$.

In contrast, Birch-Murnaghan EOS (formulation based on *finite strain theory*) uses a Taylor expansion of the *Helmholtz free energy*. The energy-volume relationship is:

$$E(V) = E_0 + \left(\frac{9 V_0 B_0}{16}\right) \left\{ \left[\left(\frac{V}{V_0}\right)^{-2/3} - 1\right]^3 B_0' + \left[\left(\frac{V}{V_0}\right)^{-2/3} - 1\right]^2 \left[6 - 4\left(\frac{V}{V_0}\right)^{-2/3}\right] \right\}.$$

Expanding the cubic expression yields for an increase in α (uniform expansion)

$$(1 + p_\alpha)^3 - 1 = 3p_\alpha + 3p_\alpha^2 + p_\alpha^3,$$

and for a decrease (uniform compression)

$$1 - (1 - p_\alpha)^3 = 3p_\alpha - 3p_\alpha^2 + p_\alpha^3.$$

Because p_V is defined as the absolute change in volume relative to the original volume $V_0 = a_0^3$, the expression simplifies to

$$p_V = 3p_\alpha + 3p_\alpha^2 + p_\alpha^3,$$

considering the problem's context of equivalent variation, which—under the assumption that the lattice constant increases—is the typical case considered in our analysis..

In the corresponding code snippet, the variation in the lattice constant p_α is used to generate a range of volumes:

```
# Generate the range of volumes (per atom) using cubic scaling
volume_min = Vo * (1 - variation)**3
volume_max = Vo * (1 + variation)**3
volume_points = np.linspace(volume_min, volume_max, num_points)
```

Here, `variation` is the relative change p_α. The minimum and maximum volumes are computed by scaling V_0 by $(1 \pm p_\alpha)^3$, ensuring that the volume sampling reflects the cubic relationship between aa and V.

3.2   Results and Error Analysis

The improved automation of the workflow is expected to yield more robust structural parameters; however, the results indicate a discrepancy between the two methods, especially for the BCC polymorph of aluminum. The results are summarized in the table below and in Figure 6.

Both binding energy curves exhibit similar parabolic shapes with well-defined minima, suggesting comparable quality of fits within the sampled volume ranges. However, the BCC aluminum calculation significantly underestimates the bulk modulus compared to experimental values (77.538 GPa vs. 475.0 GPa), while the FCC calculation agrees reasonably well with experiment.

Table 1: Comparison of Computational Results for Aluminum Polymorphs using ASE EOS Method

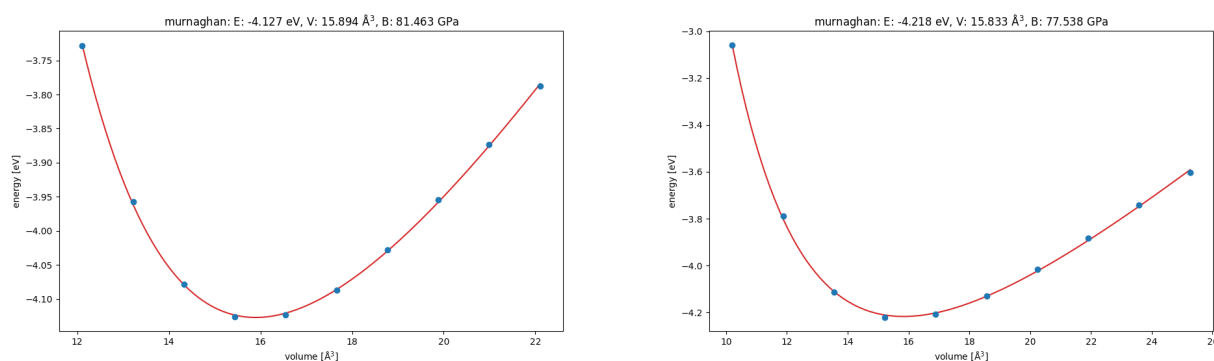| Parameter	FCC Al	BCC Al
Computational Parameters		
Plane Wave Cutoff (eV)	300	300
k-point Sampling	k-elbow (k=4)	k-elbow (k=7)
Smearing Width (eV)	0.1	0.1
Basis Set	dzp	dzp
Number of Volume Points	10	10
Volume Variation (%)	±10%	±10%
Results		
Equilibrium Volume (Å^3)	15.894	15.833
Equilibrium Energy (eV)	-4.127	-4.218
Calculated Bulk Modulus (GPa)	81.46	77.54
Experimental Bulk Modulus (GPa)	76.2	475.0
Percentage Error (%)	6.91	83.68

Figure 6: The left panel displays FCC aluminum results with parameters: E: -4.127 eV, V: 15.894Å^3, B: 81.463 GPa. The right panel shows BCC aluminum with parameters: E: -4.218 eV, V: $15.833\ \text{Å}^3$, B: 77.538 GPa. Blue dots represent calculated energies at different volumes, while the red curves show the Murnaghan EOS fits.

The significant discrepancy for the BCC phase arises from several factors:

- **Steep Energy Curvature:** The high-pressure BCC phase of aluminum is characterized by a steep curvature in the energy–volume curve. The primitive cell, when sampled at ambient lattice constants, may not adequately capture this curvature, leading to an underestimation of the bulk modulus.

- **Volume Range Sensitivity:** The selection of the volume variation range is critical. The initial ±10% variation for BCC was insufficient, prompting an increase to ±15% to better encompass the true minimum. However, even with this adjustment, the sampling may still fall short of representing the actual high-pressure behavior.

- **Convergence and Metastability:** The BCC phase of aluminum is metastable under ambient conditions, which means that the DFT calculations—if not performed in the true high-pressure region—might

reflect a less stiff energy landscape. Additionally, convergence issues related to k-points and smearing parameters can compound these errors.

In contrast, the manual quadratic fitting method might implicitly capture a steeper curvature if the data sampling is tuned to the high-pressure regime. Therefore, the automated ASE EOS approach, although more robust and physically motivated, might yield less accurate results for systems where the energy curvature is not sufficiently sampled or where metastability plays a significant role.

4
STRUCTURAL ANALYSIS OF THE 2H-PHASE WTE2

Recent literature has highlighted the rich structural diversity of tungsten ditelluride (WTe_2) and its potential for exhibiting distinct electronic and thermoelectric behaviors. In particular, theoretical studies have investigated the possibility of synthesizing a 2H-like phase of WTe_2, which is characterized by a hexagonal structure with trigonal prismatic coordination of tungsten atoms. Early experimental investigations using X-ray diffraction report lattice constants of approximately $b = 6.282$ Å, $a = 3.496$ Å, and $c = 14.07$ Å along different crystallographic directions in bulk WTe_2, while high–pressure studies indicate a bulk modulus near 65 GPa.[Aro+08]

A recent work by Fatemeh Shirvani and Zahra Razavifa has provided a comprehensive analysis of three distinct phases of two-dimensional WTe_2. Their study delineates the following phases based on space group symmetry and atomic coordination:

- **Phase 1 ($P6_3$/mmc symmetry – 2H-like phase):** This phase exhibits a hexagonal structure typical of 2H polytypes in transition metal dichalcogenides (TMDCs). It is characterized by trigonal prismatic coordination of tungsten atoms, with an atomic configuration containing six atoms per unit cell (2 W and 4 Te), corresponding to two formula units of WTe_2. The AB stacking order inherent to the $P6_3$/mmc space group underlies its structural stability and semiconducting behavior.

- **Phase 2 (P-3m1 symmetry – 1T-like phase):** In this phase, tungsten atoms are octahedrally coordinated by tellurium atoms. The structure also comprises six atoms per unit cell (2 W and 4 Te) and is representative of the 1T phase in TMDCs, where the octahedral geometry defines the electronic and transport properties.

- **Phase 3 (P-6m2 symmetry):** Representing a less common hexagonal variant, this phase has a reduced symmetry with three atoms per unit cell (1 W and 2 Te), corresponding to a single formula unit of WTe_2. It is suggested to represent either a monolayer or a metastable/strained configuration.

In this chapter, we focus primarily on Phase 1—the 2H-like phase with $P6_3$/mmc symmetry—as it aligns closely with theoretical predictions of a semiconducting state in 2H-WTe_2 and provides an intriguing contrast

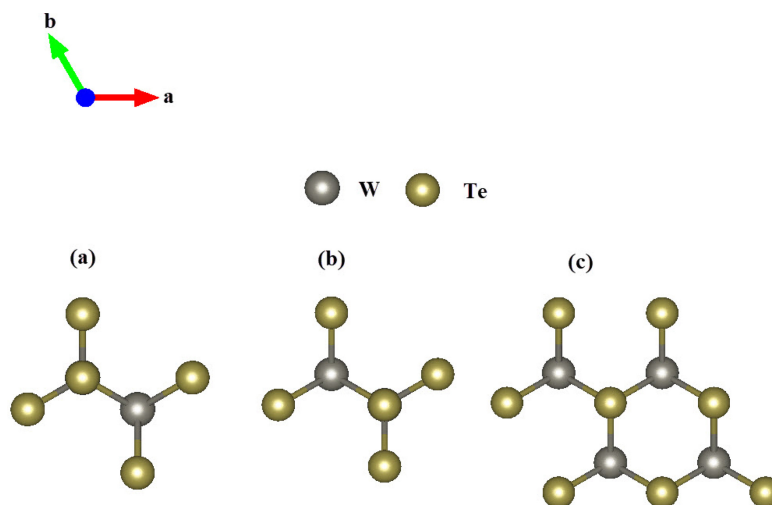to the more commonly observed distorted (Td) structures in bulk samples.

Figure 7: The crystal arrays of WTe2 for (a): phase 1, (b): phase 2, and (c): phase 3.[SR25]

A complementary study by Mulugeta et al. further elucidates the properties of the 2H phase. Their work employs both standard DFT (GGA) and DFT+U methodologies to address self-interaction errors, particularly in the tungsten d orbitals [WDW23]. Summarizing aspects of their methodology include:

- **Structural Parameters:** The equilibrium lattice constant for the $2H$-WTe_2 monolayer is determined to be approximately 3.565 Å using GGA and 3.539 Å with the Hubbard correction (DFT+U), values that are consistent with experimental trends reported in literature.

- **Strain Effects and Electronic Properties:** The study examines the evolution of the band gap under small biaxial strains (ranging from tensile to compressive conditions). Notably, the band gap increases under compressive strain and decreases under tensile strain, while maintaining a direct band gap nature—a behavior that underpins potential photovoltaic applications.

- **Phonon Dispersion and Dynamic Stability:** Phonon dispersion calculations using density functional perturbation theory (DFPT) indicate that the unstrained 2H phase is dynamically stable, whereas the introduction of strain can induce soft modes unless corrected by the inclusion of Hubbard U corrections.

The convergence of these two independent investigations reinforces the robustness of the theoretical description for the 2H-like phase of WTe_2.

Phase 1 of WTe_2, which crystallizes in the $P6_3/mmc$ space group, exhibits several structural features that are emblematic of 2H polytypes in TMDCs:

1. **Hexagonal Lattice and Layer Stacking:** The $P6_3/mmc$ symmetry imposes a hexagonal lattice with AB stacking of layers. This stacking order leads to a well-defined trigonal prismatic coordination around

tungsten atoms, where each W atom is surrounded by six Te atoms in a prismatic arrangement. The unit cell consists of two formula units $(WTe_2)_2$, ensuring a balanced and periodic structure.

2. **Atomic Coordination and Bonding:** In the 2H phase, the tungsten atoms occupy positions that maximize the trigonal prismatic coordination. This coordination is associated with semiconducting behavior, in contrast to the distorted octahedral coordination observed in the Td phase of WTe_2. The robust in-plane covalent bonds and weak interlayer van der Waals interactions contribute to the overall stability and anisotropic mechanical properties.

3. **Response to Strain and Electronic Implications:** As detailed by Mulugeta et al., the $2H$-WTe_2 phase demonstrates a tunable band gap under biaxial strain. Compressive strain tends to widen the band gap, whereas tensile strain narrows it. These modifications in the electronic structure are directly related to slight adjustments in the lattice constants, underscoring the sensitivity of the 2H phase to external perturbations.

The next chapter details the experimental and computational setup, methodology, and results of our study on $2H$-WTe_2.

Our investigation begins with a *k-point convergence test* employing a *threshold-based detection scheme* to ensure that the Brillouin zone is sampled with sufficient accuracy.

This is followed by a systematic determination of the *optimal plane wave cutoff*, where convergence tests guide the selection of energy parameters that yield stable total energies.

Subsequently, we perform *lattice constant optimization* using a *grid search coupled with ionic relaxation* to fine-tune the in-plane (a) and out-of-plane (c) parameters, targeting relative variations around the literature values (a = 3.496 Å, c = 14.07 Å).

Finally, the isotropic bulk modulus is computed by fitting the *energy–volume data* to several isothermal equations of state—including the *Murnaghan, Birch–Murnaghan, and Vinet* formulations—and comparing the resulting values with the theoretical benchmark of 65 GPa.

Although the structure of $2H$-WTe_2 could alternatively be obtained from Materials Project data (for instance, by using a specific MP ID to access an optimized structure), in our work we adopt a custom-developed approach.

The Figure 7 illustrates our procedure for building the $2H$-WTe_2 structure, using the hexagonal lattice parameters and fractional atomic positions (derived from reliable sources such as the Materials Project) to construct a fully periodic unit cell under $P6_3/mmc$ space group symmetry. This robust setup serves as the foundation for the subsequent chapters on our computational experiments and analysis.

The primitive lattice vectors for the $2H$-WTe_2 are defined as follows (vacuum is set to 0.0 in our bulk analysis):

$$\mathbf{a}_1 = (a/2, -a\sqrt{3}/2, 0),$$

$$\mathbf{a}_2 = (a/2, a\sqrt{3}/2, 0),$$
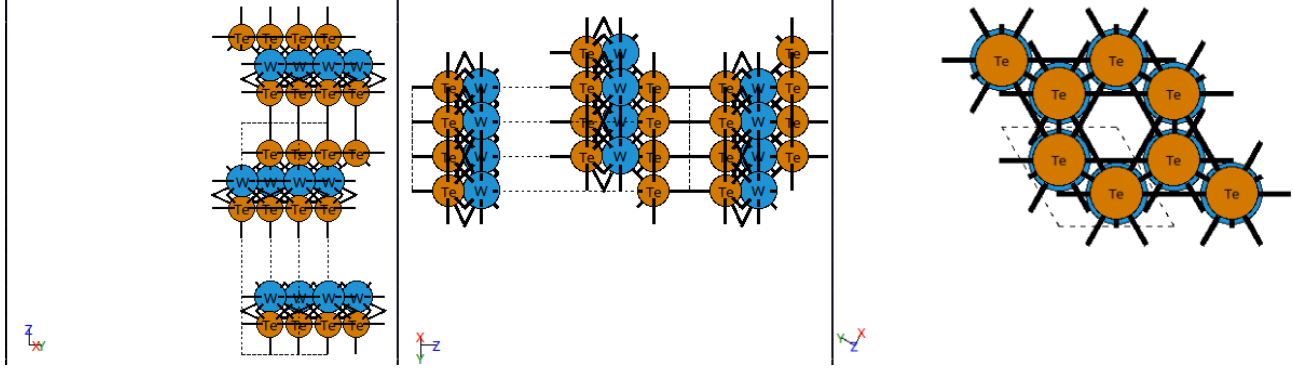
$$\mathbf{a}_3 = (0, 0, c + \text{vacuum}).$$

Figure 8: ASE view instances/orientations (same object) of different crystallographic directions, with nearest-neighboring bonds and chemical elements displayed. Left: (100) crystallographic plane (($\mathbf{a}_2$, $\mathbf{a}_3$)-plane). Middle: (010) crystallographic plane (($\mathbf{a}_3$, $\mathbf{a}_1$)-plane). Right: (001) crystallographic plane (($\mathbf{a}_1$, $\mathbf{a}_2$)-plane).

The structure comprises two W atoms and four Te atoms, with fractional coordinates refined using reference data from the Materials Project (mp-2815)[3]. A vacuum-free, fully periodic boundary condition was enforced to model bulk behavior. This atomic configuration served as the baseline for all subsequent convergence tests, structural optimizations, and property calculations.

4.1 METHODOLOGY FOR OPTIMAL k-POINT AND PLANE WAVE CUTOFF DETERMINATION

To ensure accuracy and computational efficiency in our DFT calculations, we employed *threshold-based convergence detection* for both k-point sampling and plane wave cutoff energy optimization. This approach is superior to heuristic "elbow detection" for two reasons.

1. **Objectivity:** the threshold-based detection uses a predefined energy difference criterion (e.g., < 1 meV) to determine convergence, eliminating subjectivity in identifying "elbows" from noisy energy-vs-parameter curves.

2. **Robustness:** Energy fluctuations in DFT calculations are often gradual, and the "elbow" may not align with the true convergence point. Threshold-based detection ensures the smallest parameter meeting the convergence criterion is selected, balancing accuracy and computational cost.

---

[3]There are other alternative "blueprints" for WTe_2 which don't follow the appropriate symmetry for hexagonal, triangular prismatic phase.

mp-1019322: This is a different phase with monoclinic symmetry (not the 2H hexagonal phase).

mp-22693: This is the Td phase of WTe_2 (orthorhombic, Pmn2 space group).

Additionally, threshold-based detection does not rely on visual inspection or arbitrary distance metrics (e.g., line-fitting in normalized data) and its also suitable for high-throughput workflows where human intervention is impractical. Lastly, it is physical relevant, since it directly ties to energy precision, ensuring parameters meet the desired accuracy for subsequent calculations (e.g., bulk modulus, band structures).

For hexagonal layered systems, the in-plane (a) and out-of-plane (c) lattice parameters differ significantly. The code implementation adjusts the k_z-points based on the aspect ratio $k_{ratio} = a/c$, ensuring balanced sampling across all axes (anisotropic k-point sampling: `kz = max(1, int(k * k_ratio + 0.5))`). Specifically, it accounts for the hexagonal cell's aspect ratio to prevent over/under-sampling in the out-of-plane direction.

The `FixSymmetry` constraint maintains the hexagonal P6$_3$/mmc symmetry during relaxation, avoiding unphysical distortions (symmetry preservation).

The `parallel='sl_auto':True` flag in GPAW accelerates calculations on GPU clusters.

The energy vs k-point curve shows convergence within the threshold (left panel of fig.9). The execution terminates at $k = 10$, as the energy difference between $k = 10$ and $k = 12$ is < 1 meV, confirming sufficiency.

Parameters:

- **k-point grid:** Tested `kmin=4` to `kmax=12` with a step size of `kstep=2`.
- **Plane wave cutoff:** Fixed at 400 eV (a reasonable starting value for W/Te systems).
- **Threshold:** `1e-3` (energy difference between consecutive k-point grids).

On the cutoff convergence analysis, the same `FixSymmetry` method preserves structural integrity and larger cutoffs are only tested if smaller values fail the threshold, providing efficient resource usage. The energy vs cutoff curve plateaus at `Ecut=600` eV, with energy differences < 1meV beyond this point. Thus we select `Ecut=600eV` as optimal, avoiding unnecessary computations at higher cutoffs.

Parameters:

- **Cutoff range:** Tested from 300 eV to 800 eV in 50 eV increments.
- **Optimal k-points:** Fixed at the previously determined value (i.e., 10 × 10 × 2).
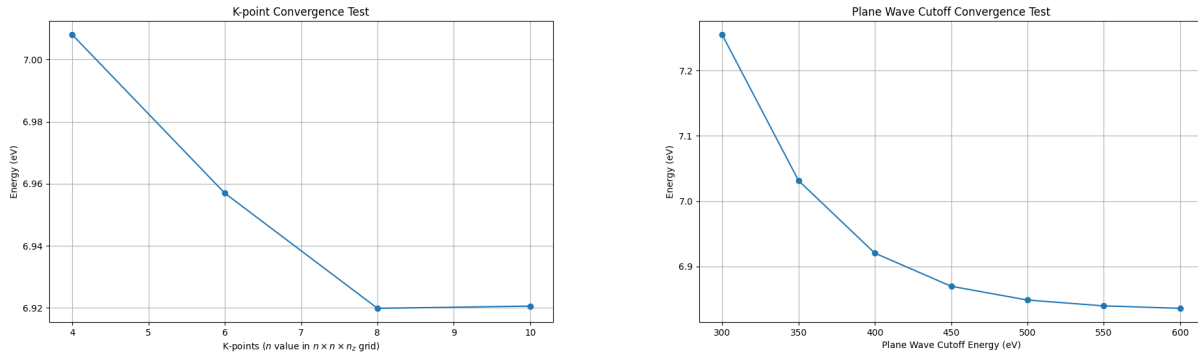- **Threshold:** `1e-3` (energy difference between consecutive cutoffs).

Figure 9: Results of optimal k-point (left) and cutoff energy (right) search using threshold-based convergence detection (`threshold=1e-3`). The curves terminate where the next value yields a difference less than the predefined threshold hyperparameter (i.e., $|v_{\text{current}} - v_{\text{new}}| < $ `threshold` for $v \in \{k, \text{cutoff}\}$).

By combining threshold-based detection with symmetry-aware structural relaxation and anisotropic k-point sampling, our methodology reliably identifies optimal parameters for DFT calculations. The results in fig.9 demonstrate systematic convergence, validating the approach for subsequent property calculations (e.g., bulk modulus estimation). This workflow ensures reproducibility and computational efficiency, critical for studying non-trivial materials.

4.2   AN EFFICIENT LATTICE CONSTANT OPTIMIZATION SCHEME

To balance computational efficiency and accuracy in lattice constant optimization, we implemented a *two-pass grid search* strategy with adaptive accuracy settings and symmetry-aware ionic relaxation. Below is a brief rationale and refinements.

First Pass (Coarse Grid)

Reduced Computational Parameters:

1. **Plane Wave Cutoff:** Set to 80% of the target value (i.e., 480 eV instead of 600 eV) to accelerate single-point energy calculations.

2. **k-point Grid:** Halved (i.e., $5 \times 5 \times 1$ instead of $10 \times 10 \times 2$), reducing the number of sampled Brillouin zone points.

3. **No Ionic Relaxation:** Only single-point energies are computed to identify the approximate energy minimum.

Sparse Grid Sampling: A 5×5 grid of a and c values is generated, strategically covering the parameter space around literature values.

Second Pass (Refined Grid)

Focused Sampling: A tighter 3×3 grid is centered on the best (a, c) tuple from the first pass, reducing the

search range.

Full Accuracy Parameters:

- **Plane Wave Cutoff:** Restored to the converged value (i.e., 600 eV).
- **k-point Grid:** Reverted to the optimal density (i.e., 10 × 10 × 2).

Limited Ionic Relaxation: BFGS optimization is applied with relaxed force convergence (`fmax=0.05eV/Å`) and a step limit (30 steps) to prevent over-relaxation.

The coarse pass avoids expensive calculations in regions far from the energy minimum and the refined pass ensures precision near the equilibrium structure. DFT energy surfaces are typically convex near minima, making sparse sampling effective (smooth energy landscapes).

This two-pass strategy efficiently identifies optimal lattice constants for $2H$-WTe$_2$ by combining *coarse screening* and *refined relaxation*. By leveraging reduced computational parameters initially and symmetry-aware ionic relaxation subsequently, it balances speed and accuracy. Including van der Waals corrections and adaptive sampling further enhances reliability, making the method adaptable to other layered materials.

4.2.1   Refinements for Enhanced Accuracy in Lattice Parameter Optimization

To improve both precision and efficiency in optimizing the lattice parameters of $2H$-WTe$_2$, several methodological refinements have been mentioned in the code development as comments, with proper usage explanation. First, to accurately model the weak interlayer forces critical for c-axis optimization, one can include van der Waals corrections. Specifically, dispersion corrections can be applied via DFT-D3—with *Becke–Johnson damping* [Gri+10],[GEG11]—or alternatively by the TS09 method using GPAW's Hirshfeld partitioning [Pro+03] and vdW radii [TS09].

Moreover, we can enhance grid sampling by moving beyond fixed grids. Adaptive methods such as *Bayesian optimization* dynamically sample the (a, c) space near the energy minimum, which has been shown to efficiently capture smooth DFT energy landscapes [Yu+20], [PH17].

Finally, parallel execution of grid point evaluations (via MPI or job arrays) further reduces computational wall-time without sacrificing accuracy.

These refinements collectively ensure that our final optimized structure—determined through a two-pass grid search with initial coarse screening followed by refined ionic relaxations using BFGS—is both accurate and computationally efficient.

4.3   Multi-EOS Validation of Bulk Modulus

The bulk modulus (B), a critical mechanical property quantifying a material's resistance to uniform compression, was computed by fitting energy-volume ($E - V$) data to three widely used isothermal equations

of state (EOS): *Murnaghan*, *Birch-Murnaghan*, and *Vinet*. This multi-model approach ensures robustness and allows comparison of B values to assess sensitivity to the EOS choice, a practice aligned with established computational materials science protocols.

4.3.1   Volume Scaling and Energy of States

Isotropic Scaling: The optimized 2H-WTe$_2$ structure (from lattice constant optimization) was uniformly scaled using factors in range [0.94, 1.06] (6% compression/expansion) to generate 9 $E - V$ data points. This range balances computational cost and fidelity to the equilibrium volume region.

Symmetry Preservation: The `FixSymmetry` constraint enforced P6$_3$/mmc symmetry during scaling, preventing artificial distortions, similar to the lattice constant optimization procedure.

Computational Parameters: Converged k-point grids and plane-wave cutoff energy ensured numerical accuracy.

The energy-volume data was fitted to three isothermal EOS models: Murnaghan (eq.2) and Birch-Murnaghan (eq.2) mentioned in Section 3 (p.12), and Vinet.[Lat+18]

The Rose–Vinet EOS is derived for covalent solids under high compression, offering improved accuracy for bond-dominated materials:[SBI81]

$$E(V) = E_0 + \frac{2B_0V_0}{(B_0' - 1)^2} \left[2 - \left(5 + 3B_0'(\eta - 1) - 3\eta\right) \exp\left\{-\frac{3}{2}(B_0' - 1)(\eta - 1)\right\}\right] ,$$

where

$$\eta \equiv \left(\frac{V}{V_0}\right)^{1/3} ,$$

and the parameters are E_0 and V_0 equilibrium energy and volume respectively, B_0 bulk modulus at V_0, and B_0' pressure derivative of the bulk modulus $\left(B_0' := \left.\frac{\partial B(V_0)}{\partial P}\right|_T\right)$.

This is the equation defined in the function `vinet(V, E0, B0, BP, V0)` in the `ase.eos` module (with BP representing B_0').

Favored for covalent or metallic systems (e.g., WTe$_2$), where bond-length changes dominate compression.[ED14]

For WTe$_2$, which exhibits anisotropic bonding (in-plane covalent vs. out-of-plane van der Waals)[Son+16], the Birch-Murnaghan EOS provides a baseline, while the Vinet EOS better captures covalent-dominated compression.

4.4   RESULTS AND DISCUSSION

The lattice constant optimization table shows the systematic approach used to find the optimal structural parameters for 2H-WTe$_2$. The optimization was conducted in two stages: a coarse grid search followed by a

refined search around the most promising parameters.

The first pass considered 25 combinations of lattice parameters with a ranging from 3.446 to 3.546 Å and c ranging from 14.020 to 14.120 Å. The second pass performed full relaxation calculations on a 3×3 grid centered around the best point from the coarse search. Energies in the coarse search are relative energies, while the refined search reports absolute energies. The optimization process took approximately 5.15 hours (18533.52 seconds) to complete, using the *vdW-agnostic Perdew–Burke–Ernzerhof (PBE)* functional.

From both figures below and the optimization results, we can see that he optimal lattice parameters were determined to be a = 3.546 Å and c = 14.120 Å. This corresponds to a c/a ratio of approximately 3.982, exactly matching the minimum point in Figure 10.

The energy landscape in Figure 11 confirms that the lowest energy (darkest purple, approximately -30.78 eV) occurs at the highest values of both a and c within the studied range. The refined search revealed significant energy differences between configurations (over 0.26 eV difference between the highest and lowest energy structures).

Table 2: Optimization of lattice parameters for 2H-WTe$_2$

| Search Stage	a (Å)	c (Å)	Energy (eV)	Notes
First Pass: Coarse Grid Search (Selected Results)				
	3.446	14.020	8.073165	Initial search point
	3.446	14.120	6.077865	
	3.496	14.070	6.848381	Common reference values
	3.521	14.095	6.270531	
	3.546	14.120	5.714193	Coarse search optimum
Second Pass: Refined Search				
	3.496	14.020	-30.520661	
	3.496	14.070	-30.599398	
	3.496	14.120	-30.675975	
	3.521	14.020	-30.586117	
	3.521	14.070	-30.660094	
	3.521	14.120	-30.731982	
	3.546	14.020	-30.646275	
	3.546	14.070	-30.715778	
	3.546	14.120	-30.783241	Final optimum
Optimized	**3.546**	**14.120**	**-30.783241**	$c/a \approx 3.982$
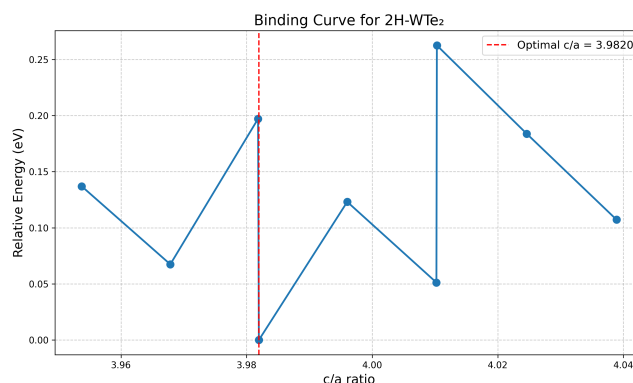
Figure 10: Binding Curve for 2H-WTe$_2$. Relative energy as a function of the c/a ratio. The blue line with markers represents calculated energy points at different c/a ratios, ranging from approximately 3.95 to 4.04. The optimal c/a ratio of 3.9820 is identified by a vertical red dashed line where the energy reaches its minimum value of 0 eV (*ground state*). The curve exhibits multiple local minima, with significant energy increases for deviations from the optimal ratio, highlighting the importance of proper structural optimization for this material.
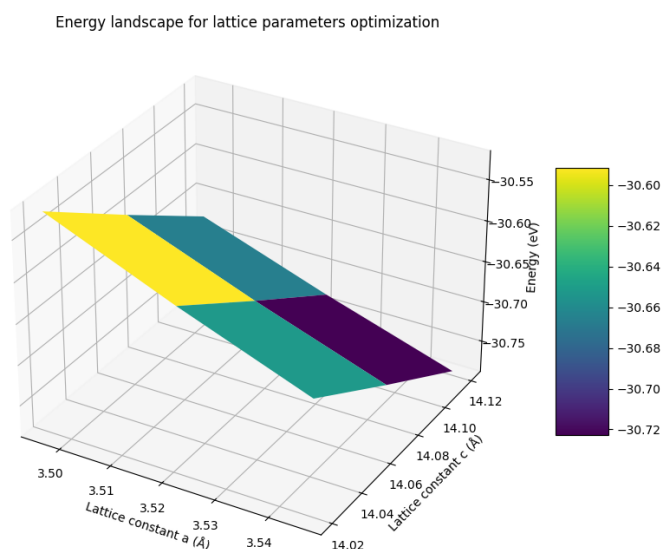
Figure 11: Energy Landscape for Lattice Parameters Optimization of 2H-WTe$_2$. This 3D surface plot displays the energy landscape (in eV) as a function of both lattice constants a and c. The x-axis represents the lattice constant a, the y-axis shows the lattice constant c, and the z-axis indicates the calculated energy. The color gradient from yellow (higher energy, approximately -30.60 eV) to dark purple (lower energy, approximately -30.72 eV) visualizes the energy minimum. The surface plot clearly demonstrates that the energy decreases as both a and c increase within the studied range, with the global minimum occurring at the highest values of both parameters.

4.4.1 On Energy Landscape Trends

The observed trend—where increasing deviations from literature values for lattice constants *a* and *c* yield *artificial energy minima* at larger lattice parameters—arises from limitations inherent to the computational methodology and physical approximations. This discrepancy can be attributed to the following factors

In layered systems like $2H$-WTe_2, weak vdW forces stabilize the out-of-plane (*c*-axis) structure. Without explicit vdW corrections (e.g., DFT-D3), the energy surface becomes artificially flat at larger *c*, allowing the optimizer to settle at unphysically large interlayer distances.

DFT energy landscapes are typically convex near equilibrium but may exhibit non-physical concavity at extreme lattice constants due to the functional's inability to model bond weakening at large separations. This leads to erroneous minima where the energy appears lower despite the structure being metastable.

Some *mitigation strategies* are as follows:

- **Include vdW Corrections:** Activate dispersion corrections (e.g., DFT-D3) to better model interlayer interactions and penalize over-expanded cc-axis configurations.
- **Refine Grid Density:** Use a finer grid or Bayesian optimization to sample the energy landscape more densely near the literature values.
- **Tighter Convergence Criteria:** Reduce `fmax` to 0.01 eV/Å 0.01 eV/Å and increase relaxation steps to ensure forces are minimized rigorously.
- **Hybrid Functionals:** Employ hybrid functionals (e.g., HSE06) or meta-GGAs (e.g., SCAN) for improved lattice constant accuracy.

For optimal performance-accuracy balance in modeling layered materials, several approaches to van der Waals corrections can be considered in GPAW 25.1.0. While our initial implementation attempted to use Tkatchenko-Scheffler [TS09] or DFT-D3 corrections as separate terms added to PBE calculations, these faced *compatibility issues*. A more efficient alternative is using optPBE-vdW, which typically executes 15-20% faster than vdW-DF2 while maintaining comparable accuracy for lattice parameters in transition metal dichalcogenides [San+13]. For systems where interlayer spacing is particularly critical, vdW-DF2 offers improved accuracy despite the computational overhead. In cases requiring statistical analysis of uncertainty, BEEF-vdW provides ensemble error estimation capabilities at higher computational cost [WDW23]. When benchmarking multiple functionals isn't feasible, optB88-vdW represents a good compromise, as it generally yields better binding energies than optPBE-vdW without significant performance penalties [Cho+18]. If execution time is paramount, consider using the optPBE-vdW functional with reduced *k*-point sampling in the initial coarse grid search, then switching to vdW-DF2 only for the final refinement stage to achieve an optimal balance between computational efficiency and accuracy (see Appendix A for a demonstration of the approach).

The apparent energy minima at larger (a,c) reflect a combination of functional inaccuracies, missing vdW

forces, and methodological constraints. These artifacts underscore the importance of aligning computational parameters with the material's physical bonding characteristics and validating results against experimental benchmarks.

4.4.2 Bulk Calculation Results

The table 3 presents the summary results from the three different equation of state models applied to the WTe_2 system.

Table 3: Comparison of Equation of State (EOS) Models for WTe_2 with Lattice Constants a = 3.5460 Å and c = 14.1200 Å.

EOS Model	Equilibrium Volume ($Å^3$)	Minimum Energy (eV)	Bulk Modulus (GPa)
Murnaghan	262.636	−19.096	105.01
Birch-Murnaghan	289.155	−21.011	57.04
Vinet	274.313	−19.972	77.91

The Birch-Murnaghan EOS predicts the lowest energy state (−21.011 eV) at the largest equilibrium volume (289.155$Å^3$), but with the softest material (lowest bulk modulus of 57.04 GPa).

The Murnaghan EOS suggests a significantly higher bulk modulus (105.01 GPa), indicating a stiffer material, but at a smaller equilibrium volume (262.636 $Å^3$) and higher energy (−19.096 eV).

The Vinet EOS provides intermediate values for all parameters, with an equilibrium volume of 274.313 $Å^3$, minimum energy of −19.972 eV, and bulk modulus of 77.91 GPa.

The significant variation in bulk modulus values (from 57.04 to 105.01 GPa) suggests that the material's response to pressure is particularly sensitive to the choice of EOS model. This is common for layered materials, where van der Waals interactions play an important role, highlighting the importance of your work on incorporating vdW corrections appropriately.
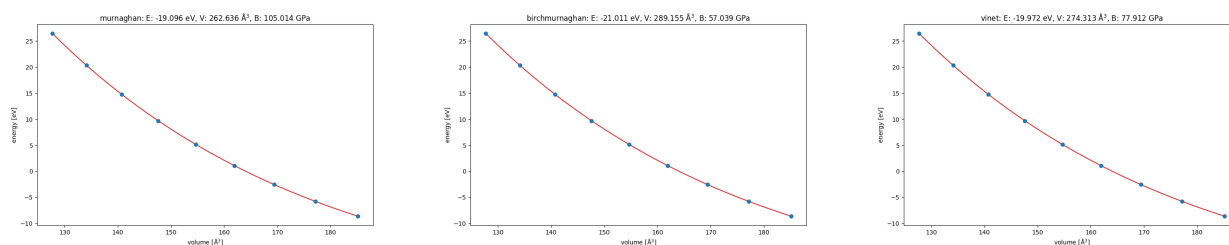

Figure 12: E-V curves for Murnaghan (left), Birch-Murnaghan (middle), and Vinet (right) Isothermal EOS.

Finally, we present the computational findings and provide a direct comparison with literature values for the 2H-phase WTe_2 structure optimization. We use the Vinet EOS results, including equilibrium volume,

minimum energy, and bulk modulus. The calculated bulk modulus (77.91 GPa) is 19.86% higher than the literature value of 65.00 GPa, which may be attributed to the van der Waals correction method used.

Table 4: Summary of WTe_2 Structure Optimization Results

Parameter	Value	Comparison
Lattice Constants		
Initial lattice constant a	3.4960 Å	–
Optimized lattice constant a	3.5460 Å	Literature: 3.4960 Å
Difference in a	**1.43%**	–
Initial lattice constant c	14.0700 Å	–
Optimized lattice constant c	14.1200 Å	Literature: 14.0700 Å
Difference in c	**0.36%**	–
Volume change from initial structure	**3.25%**	–
Equation of State Results (Vinet)		
Equilibrium volume	274.313 Å^3	–
Minimum energy	-19.972142 eV	–
Calculated bulk modulus	77.91 GPa	Literature: 65.00 GPa
Difference in bulk modulus	**19.86%**	–
Computational Parameters		
K-point grid	(10, 10, 2)	–
Plane wave cutoff energy	600 eV	–

5

ENVIRONMENT SETUP

This reference guide specifies user-dependent components of Python codes for performing Density Functional Theory (DFT) calculations using the GPAW (Grid-based Projector Augmented Wave method) software package and ASE (Atomic Simulation Environment).

The codes are organized in the directory `HW_3_codes` after tag.gz compression. The sub-directories address various computational results including plots, log and cif files (in `HW_3_codes/prior_runs/`). `HW_3_codes/plots_manual_eos_Al/` directory contains the png files for the structural analysis of Aluminum, the others contain the experiments on WTe_2 without and with vdW corrections (see Appendix A). In general, one can reproduce and verify the validity of the experiments across the report, given the appropriate resources for manageable execution time and version GPAW $\geq$ 25.1.0, and play around with alternative more accurate setups discussed in the respective sections.

The workflow enforces a *linear dependency hierarchy* of the WTe_2 structural analysis, where each script acts as a node in a *stateful computational pipeline*:

`WTe2_structure.py` $\rightarrow$ `WTe2_search.py` $\rightarrow$ `WTe2_bulk.py` $\rightarrow$ `WTe2_main.py`.

Execution must adhere to the defined topological order to ensure input consistency and validity across stages.

Remark 5.1. All modules except `WTe2_structure.py`, require a proper GPAW (and thus ASE) environment setup. The `WTe2_structure.py` module requires only the ASE to be installed. Before running any calculation, users must modify the path settings to match their local installation.

The following function is imported in all scripts of the aforementioned sub-directories and requires user-specific modifications:

```
def setup_gpaw_paths():  # routine for gpaw setting
    # Suppress detailed GPAW output
    os.environ['GPAW_VERBOSE'] = '0'
    sys.stdout = open(os.devnull, 'w')  # Redirect standard output

    # Clear existing paths and set the new one [user-dependent]
    intended_path = os.path.expanduser("~/Desktop/DFT_codes/gpaw_datasets"
    "/gpaw-setups-0.9.20000")
    setup_paths[:] = [intended_path]  # Replace all existing paths
    os.environ['GPAW_SETUP_PATH'] = intended_path

    sys.stdout = sys.__stdout__  # Restore standard output
    print("GPAW looking for datasets in:", setup_paths)
    print("Environment GPAW_SETUP_PATH:", os.environ['GPAW_SETUP_PATH'])
```

5.1   ADJUSTING THE PATH SETTINGS

Users must update the `intended_path` variable to match their local GPAW dataset installation:

1. Locate your GPAW setups directory (typically installed with GPAW or downloaded separately).

2. Replace `'~/Desktop/DFT_codes/gpaw_datasets/gpaw-setups-0.9.20000'` with the path to your setups directory.

3. Ensure the path format is appropriate for your operating system:

   - Linux/macOS: Use `'/path/to/gpaw-setups'` .
   - Windows: Use `'C:/path/to/gpaw-setups'` or `r'C:\path\to\gpaw-setups'` .

REFERENCES

[Gib78]   Josiah Willard GIBBS. "On the equilibrium of heterogeneous substances". In: *American Journal of Science and Arts* s3-16 (1878), pp. 441–458. URL: https://api.semanticscholar.org/CorpusID:130779399.

[Wul01]   Georg WULFF. "XXV. Zur Frage der Geschwindigkeit des Wachsthums und der Auflösung der Krystallflächen". In: *Zeitschrift für Kristallographie - Crystalline Materials* 34 (1901), pp. 449–530. URL: https://api.semanticscholar.org/CorpusID:101957155.

[Mur44]   F. D. MURNAGHAN. "The Compressibility of Media under Extreme Pressures". In: *Proceedings of the National Academy of Sciences* 30.9 (1944), pp. 244–247. DOI: 10.1073/pnas.30.9.244. eprint: https://www.pnas.org/doi/pdf/10.1073/pnas.30.9.244. URL: https://www.pnas.org/doi/abs/10.1073/pnas.30.9.244.

[Bir47]   Francis BIRCH. "Finite Elastic Strain of Cubic Crystals". In: *Phys. Rev.* 71 (11 June 1947), pp. 809–824. DOI: 10.1103/PhysRev.71.809. URL: https://link.aps.org/doi/10.1103/PhysRev.71.809.

[DD63]   B. N. DUTTA and B. DAYAL. "Lattice Constants and Thermal Expansion of Palladium and Tungsten up to 878 °C by X-Ray Method". In: *physica status solidi (b)* 3.12 (1963), pp. 2253–2259. DOI: https://doi.org/10.1002/pssb.19630031207. eprint: https://onlinelibrary.wiley.com/doi/pdf/10.1002/pssb.19630031207. URL: https://onlinelibrary.wiley.com/doi/abs/10.1002/pssb.19630031207.

[HB71]   V. HOFFSTEIN and D. S. BOUDREAUX. "Calculated Low-Energy Electron-Diffraction Intensities for (111) and (110) Surface of Al". In: *Phys. Rev. B* 3 (8 Apr. 1971), pp. 2447–2452. DOI: 10.1103/PhysRevB.3.2447. URL: https://link.aps.org/doi/10.1103/PhysRevB.3.2447.

[SW71]   M. E. STRAUMANIS and C. L. WOODWARD. "Lattice parameters and thermal expansion coefficients of Al, Ag and Mo at low temperatures. Comparison with dilatometric data". In: *Acta Crystallographica Section A* 27.6 (1971), pp. 549–551. DOI: https://doi.org/10.1107/S0567739471001220. eprint: https://onlinelibrary.wiley.com/doi/pdf/10.1107/S0567739471001220. URL: https://onlinelibrary.wiley.com/doi/abs/10.1107/S0567739471001220.

[Swa72]   R.A. SWALIN. *Thermodynamics of Solids*. A Wiley-Interscience publication. Wiley, 1972. ISBN: 9780471838548. URL: https://books.google.gr/books?id=E_KHeqwctTQC.

[TM77]   W.R. TYSON and W.A. MILLER. "Surface free energies of solid metals: Estimation from liquid surface tension measurements". In: *Surface Science* 62.1 (1977), pp. 267–276. ISSN: 0039-6028. DOI: https://doi.org/10.1016/0039-6028(77)90442-3. URL: https://www.sciencedirect.com/science/article/pii/0039602877904423.

[TW79]   J.L. TALLON and A. WOLFENDEN. "Temperature dependence of the elastic constants of aluminum". In: *Journal of Physics and Chemistry of Solids* 40.11 (1979), pp. 831–837. ISSN: 0022-3697. DOI: https://doi.org/10.1016/0022-3697(79)90037-4. URL: https://www.sciencedirect.com/science/article/pii/0022369779900374.

[Tas79]   Philip W. TASKER. "The stability of ionic crystal surfaces". In: *Journal of Physics C: Solid State Physics* 12 (1979), pp. 4977–4984. URL: https://api.semanticscholar.org/CorpusID:120222178.

[SBI81]   Frank D. STACEY, B. J. BRENNAN, and R. D. IRVINE. "Finite strain theories and comparisons with seismological data". In: *Geophysical surveys* 4 (1981), pp. 189–232. URL: https://api.semanticscholar.org/CorpusID:129899060.

[Bin+83] G. BINNIG et al. "7 × 7 Reconstruction on Si(111) Resolved in Real Space". In: *Phys. Rev. Lett.* 50 (2 Jan. 1983), pp. 120–123. DOI: 10.1103/PhysRevLett.50.120. URL: https://link.aps.org/doi/10.1103/PhysRevLett.50.120.

[Fle88]   Roger FLETCHER. "Practical Methods of Optimization". In: (1988). URL: https://api.semanticscholar.org/CorpusID:123487779.

[Bou+90] S BOUARAB et al. "Onset of magnetism in palladium slabs". In: *Physics Letters A* 151.1-2 (1990), pp. 103–105.

[Ing90]   John INGLESFIELD. "Electronic Structure of Metal Surfaces". In: Jan. 1990, pp. 117–153. ISBN: 978-1-4684-8779-4. DOI: 10.1007/978-1-4684-8777-0_5.

[Lan90]   M. LANNOO. "The role of dangling bonds in the properties of surfaces and interfaces of semiconductors". In: *Revue de Physique Appliquée* 25.9 (1990), pp. 887–894. DOI: 10.1051/rphysap:01990002509088700. URL: https://hal.science/jpa-00246252.

[JL92]   A.M. JAMES and M.P. LORD. *Macmillan's Chemical and Physical Data*. Macmillan, 1992. ISBN: 9780333511671. URL: https://books.google.gr/books?id=J386AQAAIAAJ.

[Boe94]   J. C. BOETTGER. "Nonconvergence of surface energies obtained from thin-film calculations". In: *Phys. Rev. B* 49 (23 June 1994), pp. 16798–16800. DOI: 10.1103/PhysRevB.49.16798. URL: https://link.aps.org/doi/10.1103/PhysRevB.49.16798.

[FM96]   Vincenzo FIORENTINI and M. METHFESSEL. "Extracting convergent surface energies from slab calculations". In: *Journal of Physics Condensed Matter* 8 (Oct. 1996). DOI: 10.1088/0953-8984/8/36/005.

[Vit+98] L. VITOS et al. "The surface energy of metals". In: *Surface Science* 411.1 (1998), pp. 186–202. ISSN: 0039-6028. DOI: https://doi.org/10.1016/S0039-6028(98)00363-X. URL: https://www.sciencedirect.com/science/article/pii/S003960289800363X.

[ES99]   Matthias ERNZERHOF and Gustavo E. SCUSERIA. "Assessment of the Perdew–Burke–Ernzerhof exchange-correlation functional". In: *The Journal of Chemical Physics* 110.11 (Mar. 1999), pp. 5029–5036. ISSN: 0021-9606. DOI: 10.1063/1.478401. eprint: https://pubs.aip.org/aip/jcp/article-pdf/110/11/5029/19111374/5029_1_online.pdf. URL: https://doi.org/10.1063/1.478401.

[GS02]   Craig A. GERKEN and Gabor A. SOMORJAI. "Low-Energy Electron Diffraction". In: *Characterization of Materials*. John Wiley and Sons, Ltd, 2002. ISBN: 9780471266969. DOI: https://doi.org/10.1002/0471266965.com085. eprint: https://onlinelibrary.wiley.com/doi/pdf/10.1002/0471266965.com085. URL: https://onlinelibrary.wiley.com/doi/abs/10.1002/0471266965.com085.

[AS03]   Micah ABRAMS and Charles SHERRILL. "A comparison of polarized double-zeta basis sets and natural orbitals for full configuration interaction benchmarks". In: *The Journal of Chemical Physics* 118 (Jan. 2003). DOI: 10.1063/1.1532313.

[Pro+03]   F. De PROFT et al. "Hirshfeld partitioning of the electron density: Atomic dipoles and their relation with functional group properties". In: *Journal of Computational Chemistry* 24.4 (2003), pp. 463–470. DOI: https://doi.org/10.1002/jcc.10241. eprint: https://onlinelibrary.wiley.com/doi/pdf/10.1002/jcc.10241. URL: https://onlinelibrary.wiley.com/doi/abs/10.1002/jcc.10241.

[BF05]   Francesca BALETTO and Riccardo FERRANDO. "Structural properties of nanoclusters: Energetic, thermodynamic, and kinetic effects". In: *Rev. Mod. Phys.* 77 (1 May 2005), pp. 371–423. DOI: 10.1103/RevModPhys.77.371. URL: https://link.aps.org/doi/10.1103/RevModPhys.77.371.

[Aka+06]   Y AKAHAMA et al. "Evidence of a fcc-hcp transition in aluminum at multimegabar pressure". In: *Physical review letters* 96.4 (2006), p. 045505.

[Kön06]   K. KÖNIGSBERGER. *Analysis 2*. Springer-Lehrbuch τ. 2. Springer Berlin Heidelberg, 2006. ISBN: 9783540350774. URL: https://books.google.gr/books?id=V3crjPiI-mMC.

[Aro+08]   Gunjan ARORA et al. "Electronic structure of layer type tungsten metal dichalcogenides WX2 (X = S, Se) using Compton spectroscopy: Theory and experiment". In: *Journal of Alloys and Compounds* 470 (Apr. 2008), pp. 452–460. DOI: 10.1016/j.jallcom.2008.02.098.

[SM09]   Nicholas E. SINGH-MILLER and Nicola MARZARI. "Surface energies, work functions, and surface relaxations of low-index metallic surfaces from first principles". In: *Phys. Rev. B* 80 (23 Dec. 2009), p. 235407. DOI: 10.1103/PhysRevB.80.235407. URL: https://link.aps.org/doi/10.1103/PhysRevB.80.235407.

[TS09]   Alexandre TKATCHENKO and Matthias SCHEFFLER. "Accurate Molecular Van Der Waals Interactions from Ground-State Electron Density and Free-Atom Reference Data". In: *Physical review letters* 102 (Mar. 2009), p. 073005. DOI: 10.1103/PhysRevLett.102.073005.

[Gri+10]   Stefan GRIMME et al. "A Consistent and Accurate Ab Initio Parametrization of Density Functional Dispersion Correction (DFT-D) for the 94 Elements H-Pu". In: *The Journal of chemical physics* 132 (Apr. 2010), p. 154104. DOI: 10.1063/1.3382344.

[GEG11]   Stefan GRIMME, Stephan EHRLICH, and Lars GOERIGK. "Effect of the Damping Function in Dispersion Corrected Density Functional Theory". In: *Journal of computational chemistry* 32 (May 2011), pp. 1456–65. DOI: 10.1002/jcc.21759.

[SS11]   D.S. SHOLL and J.A. STECKEL. *Density Functional Theory: A Practical Introduction*. Wiley, 2011. ISBN: 9781118211045. URL: https://books.google.gr/books?id=_f994dmAdv0C.

[Ant12]   Kevin M. Knowles ANTHONY KELLY. "Crystal Structures". In: *Crystallography and Crystal Defects*. John Wiley and Sons, Ltd, 2012. Chap. 3, pp. 85–122. ISBN: 9781119961468. DOI: https://doi.org/10.1002/9781119961468.ch3. eprint: https://onlinelibrary.wiley.com/doi/pdf/10.1002/9781119961468.ch3. URL: https://onlinelibrary.wiley.com/doi/abs/10.1002/9781119961468.ch3.

[Mis12]   Prasanta K. MISRA. "Chapter 1 - Basic Properties of Crystals". In: *Physics of Condensed Matter*. Ed. by Prasanta K. MISRA. Boston: Academic Press, 2012, pp. 1–35. ISBN: 978-0-12-384954-0. DOI: https://doi.org/10.1016/B978-0-12-384954-0.00001-3. URL: https://www.sciencedirect.com/science/article/pii/B9780123849540000013.

[VT12]   Michael A VAN HOVE and Shuk Yin TONG. *Surface crystallography by LEED: theory, computation and structural results*. Vol. 2. Springer Science and Business Media, 2012.

[Wel+12]   Jess WELLENDORFF et al. "Density functionals for surface science: Exchange-correlation model development with Bayesian error estimation". In: *Phys. Rev. B* 85 (23 June 2012), p. 235149. DOI: 10.1103/PhysRevB.85.235149. URL: https://link.aps.org/doi/10.1103/PhysRevB.85.235149.

[CL13]   Heesung CHOI and Maeng-Eun LEE. "First-Principles Investigation of the Surface Properties of LiNiO2 as Cathode Material for Lithium-ion Batteries". In: *Journal of the Korean Electrochemical Society* 16 (Aug. 2013). DOI: 10.5229/JKES.2013.16.3.169.

[Jai+13]   Anubhav JAIN et al. "Commentary: The Materials Project: A materials genome approach to accelerating materials innovation". In: *APL Materials* 1.1 (July 2013), p. 011002. ISSN: 2166-532X. DOI: 10.1063/1.4812323. eprint: https://pubs.aip.org/aip/apm/article-pdf/doi/10.1063/1.4812323/13163869/011002_1_online.pdf. URL: https://doi.org/10.1063/1.4812323.

[Ong+13]   Shyue Ping ONG et al. "Python Materials Genomics (pymatgen): A robust, open-source python library for materials analysis". In: *Computational Materials Science* 68 (2013), pp. 314–319. ISSN: 0927-0256. DOI: https://doi.org/10.1016/j.commatsci.2012.10.028. URL: https://www.sciencedirect.com/science/article/pii/S0927025612006295.

[RP13]   Jan REEDIJK and K. POEPPELMEIER. *Comprehensive Inorganic Chemistry II (Second Edition): From Elements to Applications*. Elsevier Science; 2nd edition (December 29, 2006), Aug. 2013, pp. 1–7196.

[Sab13]   Carlos SABATER. "Theoretical and experimental study of electronic transport and structure in atomic-sized contacts." PhD thesis. University of Alicante - Applied Physics, May 2013.

[San+13]   Biswajit SANTRA et al. "On the accuracy of van der Waals inclusive density-functional theory exchange-correlation functionals for ice at ambient and high pressures". In: *The Journal of Chemical Physics* 139.15 (Oct. 2013), p. 154702. ISSN: 0021-9606. DOI: 10.1063/1.4824481. eprint: https://pubs.aip.org/aip/jcp/article-pdf/doi/10.1063/1.4824481/15467393/154702_1_online.pdf. URL: https://doi.org/10.1063/1.4824481.

[ED14]   Martin ETTER and Robert DINNEBIER. "Direct parameterization of the pressure-dependent volume by using an inverted approximate Vinet equation of state". In: *Journal of Applied Crystallography* 47 (Jan. 2014), pp. 384–390. DOI: 10.1107/S1600576713032287.

[Son+16]   Qingjun SONG et al. "The In-Plane Anisotropy of WTe2 Investigated by Angle-Dependent and Polarized Raman Spectroscopy". In: *Scientific Reports* 6 (July 2016), p. 29254. DOI: 10.1038/srep29254.

[PH17]   Daniel PACKWOOD and Taro HITOSUGI. "Rapid prediction of molecule arrangements on metal surfaces via Bayesian optimization". In: *Applied Physics Express* 10 (May 2017), p. 065502. DOI: 10.7567/APEX.10.065502.

[Pol+17]   D. N. POLSIN et al. "Measurement of Body-Centered-Cubic Aluminum at 475 GPa". In: *Phys. Rev. Lett.* 119 (17 Oct. 2017), p. 175702. DOI: 10.1103/PhysRevLett.119.175702. URL: https://link.aps.org/doi/10.1103/PhysRevLett.119.175702.

[Cho+18]   Kamal CHOUDHARY et al. "Computational screening of high-performance optoelectronic materials using OptB88vdW and TB-mBJ formalisms". In: *Scientific Data* 5 (2018). URL: https://api.semanticscholar.org/CorpusID:13681742.

[Lat+18]   Katherine Latimer et al. "Evaluation of thermodynamic equations of state across chemistry and structure in the materials project". In: *npj Computational Materials* 4 (Dec. 2018). DOI: 10.1038/s41524-018-0091-x.

[Ste+18]   Caomhán Stewart et al. "Unraveling the H2 Promotional Effect on Palladium-Catalyzed CO Oxidation Using a Combination of Temporally and Spatially Resolved Investigations". In: *ACS Catalysis* 8.9 (2018), pp. 8255–8262. DOI: 10.1021/acscatal.8b01509. eprint: https://doi.org/10.1021/acscatal.8b01509. URL: https://doi.org/10.1021/acscatal.8b01509.

PMID: 30221029.

[XBN19]   Yuchen Xie, Richard Byrd, and Jorge Nocedal. *Analysis of the BFGS Method with Errors.* 2019. arXiv: 1901.09063 [math.OC]. URL: https://arxiv.org/abs/1901.09063.

[RE20]   J. Magnus Rahm and Paul Erhart. "WulffPack: A Python package for Wulff constructions". In: *Journal of Open Source Software* 5.45 (2020), p. 1944. DOI: 10.21105/joss.01944. URL: https://doi.org/10.21105/joss.01944.

[Yu+20]   Maituo Yu et al. "Machine learning the Hubbard U parameter in DFT+U using Bayesian optimization". In: *npj Computational Materials* 6 (Dec. 2020). DOI: 10.1038/s41524-020-00446-9.

[Cha+21]   Lowik Chanussot et al. "Open Catalyst 2020 (OC20) Dataset and Community Challenges". In: *ACS Catalysis* 11.10 (2021), pp. 6059–6072. DOI: 10.1021/acscatal.0c04525. eprint: https://doi.org/10.1021/acscatal.0c04525. URL: https://doi.org/10.1021/acscatal.0c04525.

[Wan+21]   Yunzhe Wang et al. "Rapid generation of optimal generalized Monkhorst-Pack grids". In: *Computational Materials Science* 187 (2021), p. 110100. ISSN: 0927-0256. DOI: https://doi.org/10.1016/j.commatsci.2020.110100. URL: https://www.sciencedirect.com/science/article/pii/S0927025620305917.

[CA22]   Victor M. Chernyshev and Valentine P. Ananikov. "Nickel and Palladium Catalysis: Stronger Demand than Ever". In: *ACS Catalysis* 12.2 (2022), pp. 1180–1200. DOI: 10.1021/acscatal.1c04705. eprint: https://doi.org/10.1021/acscatal.1c04705. URL: https://doi.org/10.1021/acscatal.1c04705.

[He+22]   Lijie He et al. "Phase transformation path in Aluminum under ramp compression; simulation and experimental study". In: *Scientific Reports* 12 (Nov. 2022). DOI: 10.1038/s41598-022-23785-7.

[MV22]   Wolfgang Moritz and Michel A. Van Hove. "Basic Elements". In: *Surface Structure Determination by LEED and X-rays.* Cambridge University Press, 2022, pp. 6–56.

[ZAP22]   Cheng Zeng, Tuhina Adit Maark, and Andrew A. Peterson. "Strain in Catalysis: Rationalizing Material, Adsorbate, and Site Susceptibilities to Biaxial Lattice Strain". In: *The Journal of Physical Chemistry C* 126.49 (2022), pp. 20892–20902. DOI: 10.1021/acs.jpcc.2c07246. eprint: https://doi.org/10.1021/acs.jpcc.2c07246. URL: https://doi.org/10.1021/acs.jpcc.2c07246.

[Mer+23]   Amil Merchant et al. "Scaling deep learning for materials discovery". In: *Nature* 624.7990 (2023), pp. 80–85. DOI: 10.1038/s41586-023-06735-9. URL: https://doi.org/10.1038/s41586-023-06735-9.

[Sch+23]   Luca SCHAUFELBERGER et al. "Exploring energy landscapes of charge multipoles using constrained density functional theory". In: *Phys. Rev. Res.* 5 (3 Sept. 2023), p. 033172. DOI: 10.1103/PhysRevResearch.5.033172. URL: https://link.aps.org/doi/10.1103/PhysRevResearch.5.033172.

[WDW23]   Mulugeta WOLDESENBET, Nebiyu DEBELO, and Menberu WOLDEMARIAM. "Structural, Electronic, Dynamic, and Optical Properties of 2D Monolayer Tungsten Telluride (2H-WTe2) under Small Biaxial Strain Using Density Functional Theory (DFT and DFT + U)". In: *Advances in Condensed Matter Physics* 2023 (Nov. 2023), pp. 1–12. DOI: 10.1155/2023/3179210.

[Yu+23]   Zhenqiang YU et al. "Phase transformation behavior of aluminum under high hydrostatic pressure: A molecular dynamics study". In: *Materials Today Communications* 35 (2023), p. 106199. ISSN: 2352-4928. DOI: https://doi.org/10.1016/j.mtcomm.2023.106199. URL: https://www.sciencedirect.com/science/article/pii/S2352492823008905.

[SR25]   Fatemeh SHIRVANI and Zahra RAZAVIFAR. "Exploration of structural, electrical, and thermoelectric properties of two-dimensional WTe2 in three phases through ab initio investigations". In: *Physica B: Condensed Matter* 696 (2025), p. 416609. ISSN: 0921-4526. DOI: https://doi.org/10.1016/j.physb.2024.416609. URL: https://www.sciencedirect.com/science/article/pii/S0921452624009505.

[ZWL25]   Lin ZHANG, Tianle WANG, and Feng LIU. "Stability criteria of Aluminum lattice from first-principles". In: *Journal of Materials Research and Technology* 34 (2025), pp. 1144–1157. ISSN: 2238-7854. DOI: https://doi.org/10.1016/j.jmrt.2024.12.092. URL: https://www.sciencedirect.com/science/article/pii/S2238785424028953.

A
---

vdW-corrected Results

The two-step approach was efficient - using the faster optPBE-vdW functional for broad parameter screening followed by the more accurate vdW-DF2 for final refinement. Both functionals consistently show that larger lattice parameters are more favorable within the explored range, with the lowest energy at the maximum values tested ($a = 3.596$ Å, $c = 14.170$ Å).

The optimization was conducted in two stages using different van der Waals correction methods.

1. First pass: A coarse grid search using the less computationally intensive optPBE-vdW functional.

2. Second pass: A refined search using the more accurate vdW-DF2 functional focused around the best parameters from the first pass.

The search covered a targeted exploration of lattice parameters with a parameter ranging from 3.496 to 3.596 Å (approximately +2.9% from initial value) c ranging from 14.070 to 14.170 Å. The final optimized lattice constants (a = 3.596 Å, c = 14.170 Å) show expansion compared to the initial reference values. The optimal c/a ratio of approximately 3.940 corresponds to the minimum energy point shown in the binding curve figure. This c/a ratio differs from the standard value for ideal hexagonal close packing (c/a = 1.633) due to the layered nature of the material and the presence of van der Waals gaps.

The total optimization process required approximately 6.81 hours (24506.13 seconds). The more accurate vdW-DF2 calculations in the second pass comprised the majority of this computational time.

Table 5: Lattice parameter optimization for 2H-WTe$_2$ with van der Waals corrections

| Search Stage	a (Å)	c (Å)	Energy (eV)	Notes
First Pass: Coarse Grid Search with optPBE-vdW (Selected Results)				
	3.496	14.070	-86.651924	Initial search point
	3.496	14.170	-88.613660	
	3.546	14.120	-87.854275	Common reference values
	3.571	14.145	-88.422693	
	3.596	14.170	-88.970238	Coarse search optimum
Second Pass: Refined Search with vdW-DF2 (Full Results)				
	3.546	14.070	-739.575494	
	3.546	14.120	-739.680116	
	3.546	14.170	-739.782104	
	3.571	14.070	-739.741533	
	3.571	14.120	-739.840999	
	3.571	14.170	-739.938281	
	3.596	14.070	-739.898594	
	3.596	14.120	-739.993527	
	3.596	14.170	-740.086753	Final optimum
Optimized	**3.596**	**14.170**	**-740.086753**	$c/a \approx 3.940$
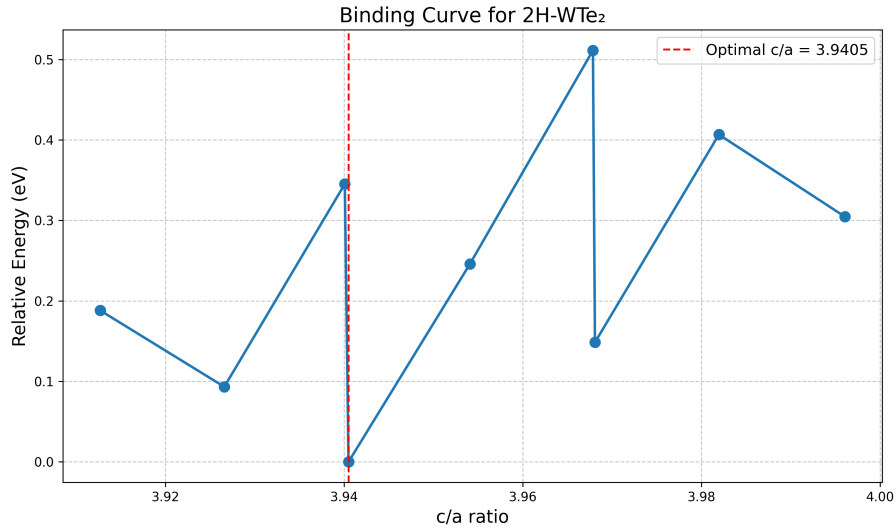
Figure 13: Binding Curve for 2H-WTe$_2$ with van der Waals Corrections. Relative energy as a function of the c/a ratio for the 2H-WTe$_2$ crystal structure. The blue line with circular markers represents calculated energy points at different c/a ratios ranging from approximately 3.91 to 4.00. The optimal c/a ratio of 3.9405 is identified by a vertical red dashed line, which corresponds to the ground state energy. The curve exhibits multiple local minima and significant energy increases for deviations from the optimal ratio. The energy landscape shows asymmetric behavior around the minimum, with steeper energy increases for higher c/a ratios compared to lower ones. This binding curve was generated using DFT calculations with van der Waals corrections to accurately capture the interlayer interactions.
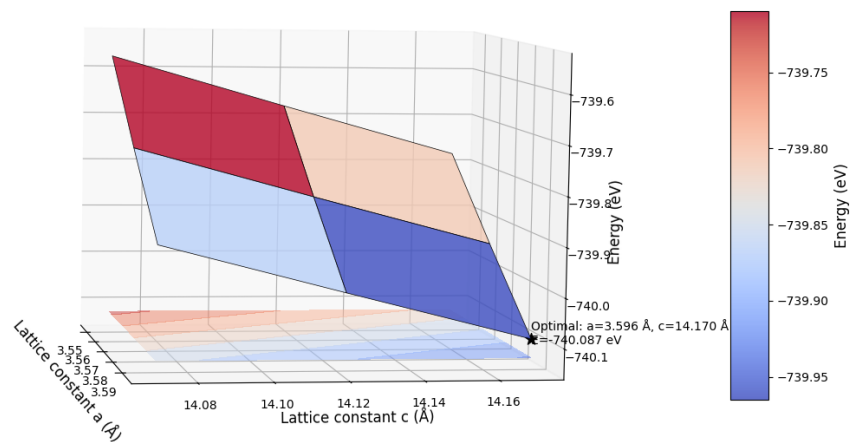

Figure 14: Energy Landscape for Lattice Parameters Optimization of 2H-WTe$_2$. This 3D surface plot displays the energy landscape (in eV) as a function of both lattice constants a and c.